Diffusion tensor MR imaging of rat glioma models: A correlation study of MR imaging and histology

Silun Wang[a,*] and **Jinyuan Zhou**[a,b]

[a]Division of MR Research, Department of Radiology, Johns Hopkins University School of Medicine, Baltimore, Maryland, USA

[b]F.M. Kirby Research Center for Functional Brain Imaging, Kennedy Krieger Institute, Baltimore, Maryland, USA

Abstract

Introduction—Diffusion tensor MR imaging (DTI) can be used to characterize the microstructures of ordered biological tissues. This study was designed to assess histological features of gliomas and surrounding brain tissues in rats using DTI.

Methods—Three types of tumors, a 9L gliosarcoma (n = 8), an F98 glioma (n = 5), and a human glioblastoma xenograft (GBM22; n = 8) were incubated in rat brains and underwent conventional MRI and DTI scanning using a 4.7 T animal MRI system. Fractional anisotropy (FA), isotropic apparent diffusion coefficient (ADC), parallel diffusivity ($\lambda_{//}$), and perpendicular diffusivity ($\lambda\perp$), as well as histological features within several regions of interest, were analyzed.

Results—All tumor masses consisted of low-FA central zones (tumor center) and high-FA peripheral regions (tumor rim). Histological examination revealed the existence of highly coherent tumor organizations (circular for 9L and F98 or radial for GBM22) in the tumor rims. There were higher ADC, $\lambda\perp$ and $\lambda_{//}$ in the peritumoral edema, compared to the contralateral grey matter. There were significantly lower FA and higher $\lambda\perp$ in the ipsilateral white matter than in the contralateral white matter for the GBM22 tumor, whereas there were no differences for the 9L and F98 tumors. Histology showed GBM22 tumor infiltration into the ipsilateral damaged white matter.

Conclusions—Quantitative analysis of DTI indices provides useful information for assessing tumor microstructures and tumor cell invasion into the adjacent gray matter and white matter.

Keywords

brain tumor; peritumoral edema; tumor infiltration; DTI

Introduction

Gliomas carry a poor prognosis, with a median survival time of 12–15 months for patients with glioblastoma multiforme, and 2–5 years for patients with anaplastic gliomas [1].

Histopathological examination is the gold standard for the diagnosis of gliomas. However, the incidence of unsuccessful biopsies has been reported at approximately 8%, which may include nonrepresentative or nondiagnostic specimens, such as inflammatory changes, gliosis, necrosis, or normal brain [2]. Even if the biopsied specimen is adequate, there is a diagnostic disagreement rate of 15% between neuropathologists [3]. In addition, it has been reported that around 6% of patients who undergo surgical biopsy of brain cancer suffer from severe complications, such as subarachnoid hemorrhage, intracerebral hemorrhage, increased edema, and severe neurological deficits. Furthermore, around 2% of patients die following the procedure [4]. A noninvasive diagnostic test to accurately assess gliomas, therefore, could potentially reduce the necessity for biopsies and their associated complications.

The primary goal in the treatment of malignant gliomas is to remove as much tumor as possible while minimizing the damage to surrounding brain tissue to preserve neuronal functions. Optimal neurosurgery and radiotherapy rely on accurate information about the local extent of a tumor and its infiltration into the brain parenchyma. These factors do not influence the choice of a treatment strategy, but ultimately, determine the prognosis of the patient. Therefore, the main purpose of noninvasive brain cancer imaging is focused on tumor localization, grade determination, and tumor infiltration characterization [5].

Magnetic resonance imaging (MRI) plays a key role in the detection, staging, and characterization of the tumor infiltration of gliomas [6–9]. However, conventional MRI imaging of gliomas has inherent limitations, such as inadequate assessment of both peritumoral edema and the integrity of the adjacent white matter. Diffusion tensor MR imaging (DTI) can measure the three-dimensional movement of water molecules *in vivo* and elucidate the microstructure of the brain tissue [10–14]. Tissue microstructural characteristics in gliomas vary considerably. Pseudopalisading necrosis is a neuropathological hallmark of glioblastoma multiforme, where the lesion necrosis is surrounded by radially arranged anaplastic cells, along with tumor cell infiltration, vascular or cytotoxic edema, and reactive gliosis in the peritumoral edema [15].

In this study, we aim to evaluate the microstructural characteristics of gliomas, peritumoral edema, and adjacent white matter using DTI in three different glioma animal models. These animal models exhibit different biological characteristics in mimicking human gliomas. We hypothesize that (i) there are distinct diffusion patterns in these animal models that correlate with the tumor microstructure, and (ii) quantification of DTI indices can characterize the peritumoral edema and the integrity of adjacent white matter.

Materials and Methods

Animal model preparation

Three tumor cell lines were used in this study, including 9L and F98 tumor models that were derived from nitrosourea-induced malignancies of glial origin [16]. A human glioblastoma cell line (randomly called GBM22) was established from resected tumors, passaged serially as tumor xenografts, and cultured briefly prior to implantation into the rat brain [17]. The 9L and F98 tumor models are well-established glioma models and their biological characteristics mimic moderately gliomas in humans [18]. However, the GBM22 tumor shares the essential characteristics of high invasiveness and poor demarcation with human glioblastomas [19]. There were 25,000 9L tumor cells ($n = 8$) or F98 glioma cells ($n = 5$) implanted in each Fisher rat, and 100,000 GBM22 cells implanted in each nude rat ($n = 8$). All the experimental procedures were approved by the Animal Care and Use Committee of the Johns Hopkins University School of Medicine.

MRI data acquisition

The rats underwent MRI scanning on day 11 ~13 (9L), days 10–11 (F98) and days 26–28 (GBM22) post-tumor implantation. The diameter of the tumors was approximately 4–5 mm. Imaging experiments were performed on a 4.7 T horizontal bore animal MR system (Bruker Biospin, MA) with an actively decoupled cross-coil setup of a 70 mm body coil for RF transmission and a 25 mm surface coil for signal reception.

In vivo multi-slice images of rat brains were acquired in the horizontal plane (5 slices, slice thickness 1.5 mm, field of view (FOV) = 42 mm × 32 mm). T_2w was acquired using a fast spin echo (FSE) sequence and the following parameters: repetition time (TR) = 3s; echo time (TE) = 64 ms; matrix = 256 × 256; and resolution = 0.16 mm × 0.17 mm. Diffusion tensor images were acquired using a multiple-slice, multiple-spin echo diffusion-weighted (DW) sequence (TR = 2 s, four echoes with TEs of 26.3/36.7/47.1/57.5 ms, matrix = 128 × 96, resolution = 0.33 mm × 0.33 mm, number of average = 4). Trapezoidal diffusion gradients were used (Δ = 14 ms, δ = 5 ms, gradient rise time = 0.4 ms, gradient strength = 14 Gauss/cm). Seven DW images with different b values were acquired (one image with b value = 50 s/mm^2 and the rest with b value = 625 s/mm^2).

Image analysis

DTI eigenvalues (λ_1, λ_2 and λ_3) were obtained using DTI Studio v2.30 [20]. Then, fractional anisotropy (FA), apparent diffusion coefficient (ADC), parallel diffusivity ($\lambda_{//}$), and perpendicular diffusivity ($\lambda\perp$) maps were created for quantitative analysis by applying the following equations:

$$FA = \sqrt{\frac{1}{2}} \frac{\sqrt{(\lambda_1 - \lambda_2)^2 + (\lambda_2 - \lambda_3)^2 + (\lambda_3 - \lambda_1)^2}}{\sqrt{\lambda_1^2 + \lambda_2^2 + \lambda_3^2}} \quad (1)$$

$$ADC = (\lambda_1 + \lambda_2 + \lambda_3)/3 \quad (2)$$

$$\lambda_{//} = \lambda_1 \quad (3)$$

$$\lambda_\perp = (\lambda_2 + \lambda_3)/2 \quad (4)$$

Regions of interest (ROIs) were manually drawn on the T_2w and DTI images. The central regions of gliomas (tumor center) were defined as hypointense on the FA maps (Fig. 1A). The peripheral regions of gliomas (tumor rim) were defined as hyperintense on the FA images [21]. Then, the peritumoral edema was defined as the hyperintense region on the T_2w images. Because the tumors were implanted in the thalamus areas, the peritumoral edema covered most of the thalamus (Fig. 1B). The contralateral grey matter (thalamus) served as a control. Finally, ipsilateral and contralateral white matter tracts were drawn in the external capsule regions on the FA maps (Fig. 1A). ImageJ 1.43n (National Institutes of Health, Bethesda, MD) was used to evaluate the quantitative indices in all of the images.

Histopathology evaluation

Rats were sacrificed for histological evaluation after MRI scanning. Brain specimens were processed using standard histological protocols. The specimens were sectioned in 10 μm thick slices and stained with hematoxylin and eosin (H&E). Histological specimens were analyzed within the regions corresponding to the quantitative MRI measurements.

Peritumoral regions were classified infiltrated or non-infiltrated, according to the boundary features between the tumor and adjacent brain parenchyma and the presence of tumor cells invading the adjacent brain parenchyma. Histological images were acquired using a light microscope under 10× – 200× magnification, at the same exposure level, by digital photomicrography.

Statistical analysis

All results are expressed as mean ± standard deviation. A paired sample t test was applied to analyze statistical differences in the DTI indices between the tumor rim and tumor center, the peritumoral edema and contralateral grey matter, as well as the ipsilateral and contralateral white matter. All statistical analysis was performed using the statistical package SPSS for Windows (Version 18, SPSS, Chicago). A p value of <0.05 was considered to be statistically significant.

Results

DTI and conventional MR imaging of gliomas

The 9L gliosarcoma was homogeneously hyperintense on T_2w images and there was a distinct boundary between the tumor and the adjacent normal parenchyma. The F98 tumor was heterogeneously hyperintense on T_2 images. No apparent boundary could be seen between the tumor and adjacent brain tissue. The GBM22 tumor was iso- to hyperintense on T_2 images. For all tumor models, peritumoral edema that covered the adjacent grey matter and white matter tracts showed hyperintensity on T_2 images. In addition, severe mass effects could be seen in the ventricular space and adjacent white matter tracts.

For all three tumor models, the FA maps showed a highly heterogeneous tumor mass (Fig. 2). There was a dark central lesion with low diffusion anisotropy, compared to the contralateral brain tissue. In contrast, a bright peripheral area with a high degree of diffusion anisotropy was observed on FA maps, as reported previously. The ADC maps were relatively homogenous, compared to FA. There were different diffusion patterns on ADC maps within GBM22 tumors, compared to 9L and F98 tumors (Fig. 2). In the 9L and F98 tumors, the ADC maps were markedly hyperintense in the tumor cores, compared to the contralateral grey matter. However, the ADC signal intensity within the GBM22 tumor was iso-intense (Fig. 2) or hyperintense, compared to the contralateral grey matter, depending on the animal.

On the ADC maps and T_2 images, peritumoral regions were clearly identifiable, with hyperintense signals. On FA maps, these peritumoral regions were hypointense, compared to the contralateral grey matter among all three tumor models, where the peritumoral white matter (external capsule) could be clearly identified, with hyperintense FA signals.

Quantitative analysis of DTI indices of the gliomas

Table 1 summarizes the DTI indices in the 9L, F98, and GBM22 glioma models. Significantly higher FA values were found in the tumor rim of F98 and GBM22 than in the tumor center (p = 0.01 and p <0.001, respectively). Further, significantly lower $\lambda\perp$ values were found in the 9L tumor rim, compared to the tumor center (p = 0.015). The F98 tumor showed significantly lower $\lambda\perp$ in the tumor rim than in the tumor center (p = 0.038). However, the GBM22 tumor had significantly higher $\lambda_{//}$ values in the tumor rim than in the tumor center (p = 0.006). In the peritumoral edema, all three glioma models showed significantly higher ADC, $\lambda\perp$ and $\lambda_{//}$ values compared to the contralateral grey matter. Notably, the GBM22 tumor had significantly lower FA, but higher $\lambda\perp$ in the ipsilateral white matter, compared to the contralateral white matter, consistent with DTI patterns of

myelin damage [22–24]. No significant differences in DTI indices were found between both sides of the white matter in 9L and F98 tumors.

Histological evaluations

There are distinct histological patterns among these three tumor models (Figs. 3–5). High densities of 9L tumor cells with randomly distributed internal space were observed within the 9L tumors. On the contrary, the F98 and GBM22 tumors showed a clear central necrosis with few tumor cells. Moreover, the high densities of tumor cells showed a unique arrangement. The individual tumor cells and adjacent interstitial space in 9L and F98 tumors formed a circular organization pattern in the tumor rim, corresponding to high diffusion anisotropy in the DTI images. Notably, the GBM22 tumor cells seemed elongated with adjacent interstitial spaces, and an apparently "streaming" radial pattern, corresponding to high FA regions. Finally, the peritumoral grey matter was compressed by the tumor mass and the tumor cells invaded the adjacent brain parenchyma at varying distances from the tumor mass. These patterns were more obvious in F98 and GBM22 tumors. With regard to the adjacent white matter (external capsule), the ipsilateral white matter in the 9L and F98 models seemed normal, compared to the contralateral white matter. However, the ipsilateral white matter of GBM22 tumors was damaged by infiltrating tumor cells. The boundary between the tumor and the adjacent white matter was unclear.

Discussion

Malignant gliomas are histologically characterized by pseudopalisading, endothelial proliferation, or glomerular formation [15]. Organized microstructures exist in solid tumor tissues, where the tumor cells proliferate rapidly and pack closely in a coherent way, as opposed to the random microstructures in necrotic or cystic areas. This is consistent with DTI findings in humans, where FA and tumor cellularity were found to be positively correlated [25, 26]. For example, Kinoshita et al. analyzed the FA values in grade II to IV gliomas and then correlated them with histology [26]. A significant positive correlation was demonstrated between the numbers of tumor cells and FA values ($r = 0.75$). Our results indicate that the solid part of gliomas (tumor rim) has a higher degree of diffusion anisotropy, compared to the tumor center with spontaneous necrosis. Histological evaluations confirmed the existence of well-arranged tumor cells in the tumor rims, which formed a circular pattern in the 9L and F98 tumors and a radial pattern in the GBM22 tumors. Although these brain tumor xenografts grow relatively fast, compared to human gliomas, our results provide useful information to better understand the growth patterns of gliomas, which is useful for the differential diagnosis and evaluation of treatment response.

Peritumoral edema can be classified as vasogenic edema, such as the edema adjacent to meningiomas and metastatic tumors, and tumor-infiltrated edema, such as the edema surrounding gliomas. The ability of diffusion MRI to differentiate vasogenic edema from tumor-infiltrated edema is still controversial. Lu et al. reported significantly higher ADC values in vasogenic edema than in tumor-infiltrated edema [27], whereas contradictory results were reported by other groups [28]. Peritumoral edema consists of several complicated pathological components, such as compressed normal parenchyma, vasogenic edema, tumor cell infiltration, and reactive astrogliosis. This may explain the conflicting reports [29]. When the tumor tissue compresses the adjacent brain parenchyma, diffusion anisotropy would increase. Several other pathological changes could decrease the diffusion anisotropy. For example, vasogenic edema can enhance the free diffusion of water in the extracellular space, infiltrating tumor cells can disrupt the integrity of adjacent white matter tracts, and reactive astrogliosis can impede the free diffusion of water due to the swelling of astrocytes. Therefore, the diffusion characteristics of peritumoral edema are determined by these pathological components. We demonstrated that all three tumors exhibit significantly

higher ADC, λ⊥ and λ// values in peritumoral edema, compared to normal grey matter. Histology showed tumor compression and vasogenic edema in 9L and F98 tumors and GBM22 tumor infiltration into the adjacent brain parenchyma. Our results indicate that DTI indices may have limitations in identifying tumor cell infiltration into the peritumoral edema.

Gliomas do not only displace the fiber bundles of the white matter, as in low-grade gliomas, but also damage the adjacent white matter tracts due to tumor cell infiltration, as in high-grade gliomas. In our models, GBM22 had significantly lower FA, together with significantly higher λ⊥ in the ipsilateral white matter, compared to the contralateral white matter. On the contrary, no significant differences were found between the ipsilateral and contralateral white matter in the 9L gliosarcoma or F98 tumor. Recent studies have demonstrated that FA and λ⊥ are sensitive and specific biomarkers, reflecting the integrity of the myelin in many pathological or physiological processes, such as white matter maturation, demyelination, or dysmyelination [22–24], since λ⊥ represents water diffusion perpendicular to the myelin sheaths. Tumor cell infiltration may induce the myelin damage. This is supported by experimental studies that show that demyelination is a major pathological change in the adjacent white matter tracts [30, 31]. Clinically, demyelination is also observed in the adjacent white matter, especially in patients with high-grade gliomas [32]. Our results show that adjacent white matter tracts were infiltrated and damaged by tumor cells in the GBM22 tumors, but were preserved in the 9L and F98 tumor models. Significantly decreased FA, along with increased λ⊥ within the ipsilateral white matter of gliomas, can be regarded as useful biomarkers to assess the integrity of adjacent white matter tracts.

In conclusion, brain tumors are highly organized. A quantitative analysis of DTI indices can provide useful information about the microstructures of brain tumors and the adjacent gray matter and white matter at a near-cellular level.

Acknowledgments

References

1. Wen PY, Kesari S. Malignant gliomas in adults. N Engl J Med. 2008 Jul 31; 359(5):492–507. [PubMed: 18669428]

2. Soo TM, Bernstein M, Provias J, et al. Failed stereotactic biopsy in a series of 518 cases. Stereotact Funct Neurosurg. 1995; 64(4):183–196. [PubMed: 8817805]

3. Murphy M, Loosemore A, Ferrer I, et al. Neuropathological diagnostic accuracy. Br J Neurosurg. 2002 Oct; 16(5):461–464. [PubMed: 12498489]

4. Bernstein M, Parrent AG. Complications of CT-guided stereotactic biopsy of intra-axial brain lesions. J Neurosurg. 1994 Aug; 81(2):165–168. [PubMed: 8027795]

5. Maier SE, Sun Y, Mulkern RV. Diffusion imaging of brain tumors. NMR Biomed. 2010 Aug; 23(7): 849–864. [PubMed: 20886568]

6. Catalaa I, Henry R, Dillon WP, et al. Perfusion, diffusion and spectroscopy values in newly diagnosed cerebral gliomas. NMR Biomed. 2006; 19:463–475. [PubMed: 16763973]

7. Verma R, Zacharaki EI, Ou Y, et al. Multiparametric tissue characterization of brain neoplasms and their recurrence using pattern classification of MR images. Acad Radiol. 2008; 15:966–977. [PubMed: 18620117]

8. Chang SM, Nelson S, Vandenberg S, et al. Integration of preoperative anatomic and metabolic physiologic imaging of newly diagnosed glioma. J Neuro-Oncol. 2009; 92:401–415.

9. Zhou J, Tryggestad E, Wen Z, et al. Differentiation between glioma and radiation necrosis using molecular magnetic resonance imaging of endogenous proteins and peptides. Nature Med. 2011; 17:130–134. [PubMed: 21170048]

10. Sinha S, Bastin ME, Whittle IR, et al. Diffusion tensor MR imaging of high-grade cerebral gliomas. AJNR Am J Neuroradiol. 2002; 23:520–527. [PubMed: 11950638]

11. Field AS, Alexander AL, Wu YC, et al. Diffusion tensor eigenvector directional color imaging patterns in the evaluation of cerebral white matter tracts altered by tumor. J Magn Reson Imag. 2004; 20:555–562.

12. Huang H, Zhang J, Wakana S, et al. White and gray matter development in human fetal, newborn and pediatric brains. NeuroImage. 2006; 33:27–38. [PubMed: 16905335]

13. Zhang J, van Zijl PCM, Laterra J, et al. Unique patterns of diffusion directionality in rat brain tumors revealed by high-resolution diffusion tensor MRI. Magn Reson Med. 2007; 58:454–462. [PubMed: 17763344]

14. Zhou, JY. Growth of malignant gliomas in vivo: High-resolution diffusion tensor magnetic resonance imaging. Hayat, MA., editor. New York: Springer; 2012.

15. Wippold FJ 2nd, Lammle M, Anatelli F, et al. Neuropathology for the neuroradiologist: palisades and pseudopalisades. AJNR Am J Neuroradiol. 2006 Nov-Dec;27(10):2037–2041. [PubMed: 17110662]

16. Barth RF, Kaur B. Rat brain tumor models in experimental neuro-oncology: The C6, 9L, T9, RG2, F98, BT4C, RT-2 and CNS-1 gliomas. J Neuro-Oncol. 2009; 94:299–312.

17. Sarkaria JN, Carlson BL, Schroeder MA, et al. Use of an orthotopic xenograft model for assessing the effect of epidermal growth factor receptor amplification on glioblastoma radiation response. Clin Cancer Res. 2006 Apr 1; 12(7 Pt 1):2264–2271. [PubMed: 16609043]

18. Kim S, Pickup S, Hsu O, et al. Diffusion tensor MRI in rat models of invasive and well-demarcated brain tumors. NMR Biomed. 2008 Mar; 21(3):208–216. [PubMed: 17530617]

19. Salhotra A, Lal B, Laterra J, et al. Amide proton transfer imaging of 9L gliosarcoma and human glioblastoma xenografts. NMR Biomed. 2008; 21:489–497. [PubMed: 17924591]

20. Jiang H, van Zijl PC, Kim J, et al. DtiStudio: resource program for diffusion tensor computation and fiber bundle tracking. Comput Methods Programs Biomed. 2006 Feb; 81(2):106–116. [PubMed: 16413083]

21. Wang W, Steward CE, Desmond PM. Diffusion tensor imaging in glioblastoma multiforme and brain metastases: the role of p, q, L, fractional anisotropy. AJNR Am J Neuroradiol. 2009 Jan; 30(1):203–208. [PubMed: 18842762]

22. Song SK, Sun SW, Ramsbottom MJ, et al. Dysmyelination revealed through MRI as increased radial (but unchanged axial) diffusion of water. NeuroImage. 2002 Nov; 17(3):1429–1436. [PubMed: 12414282]

23. Wang SL, Wu EX, Qiu DQ, et al. Longitudinal Diffusion Tensor Magnetic Resonance Imaging Study of Radiation-Induced White Matter Damage in a Rat Model. Cancer Research. 2009 Feb; 69(3):1190–1198. [PubMed: 19155304]

24. Wang S, Wu EX, Tam CN, et al. Characterization of white matter injury in a hypoxic-ischemic neonatal rat model by diffusion tensor MRI. Stroke. 2008 Aug; 39(8):2348–2353. [PubMed: 18535275]

25. Inoue T, Ogasawara K, Beppu T, et al. Diffusion tensor imaging for preoperative evaluation of tumor grade in gliomas. Clin Neurol Neurosurg. 2005 Apr; 107(3):174–180. [PubMed: 15823671]

26. Kinoshita M, Hashimoto N, Goto T, et al. Fractional anisotropy and tumor cell density of the tumor core show positive correlation in diffusion tensor magnetic resonance imaging of malignant brain tumors. Neuroimage. 2008 Oct 15; 43(1):29–35. [PubMed: 18672074]

27. Lu S, Ahn D, Johnson G, et al. Peritumoral diffusion tensor imaging of high-grade gliomas and metastatic brain tumors. AJNR Am J Neuroradiol. 2003 May; 24(5):937–941. [PubMed: 12748097]

28. Morita K, Matsuzawa H, Fujii Y, et al. Diffusion tensor analysis of peritumoral edema using lambda chart analysis indicative of the heterogeneity of the microstructure within edema. J Neurosurg. 2005 Feb; 102(2):336–341. [PubMed: 15739563]

29. Engelhorn T, Savaskan NE, Schwarz MA, et al. Cellular characterization of the peritumoral edema zone in malignant brain tumors. Cancer Sci. 2009 Oct; 100(10):1856–1862. [PubMed: 19681905]

30. Asanuma T, Doblas S, Tesiram YA, et al. Visualization of the protective ability of a free radical trapping compound against rat C6 and F98 gliomas with diffusion tensor fiber tractography. J Magn Reson Imaging. 2008 Sep; 28(3):574–587. [PubMed: 18777527]

31. Lope-Piedrafita S, Garcia-Martin ML, Galons JP, et al. Longitudinal diffusion tensor imaging in a rat brain glioma model. NMR Biomed. 2008 Oct; 21(8):799–808. [PubMed: 18470959]

32. Goebell E, Paustenbach S, Vaeterlein O, et al. Low-grade and anaplastic gliomas: differences in architecture evaluated with diffusion-tensor MR imaging. Radiology. 2006 Apr; 239(1):217–222. [PubMed: 16484348]
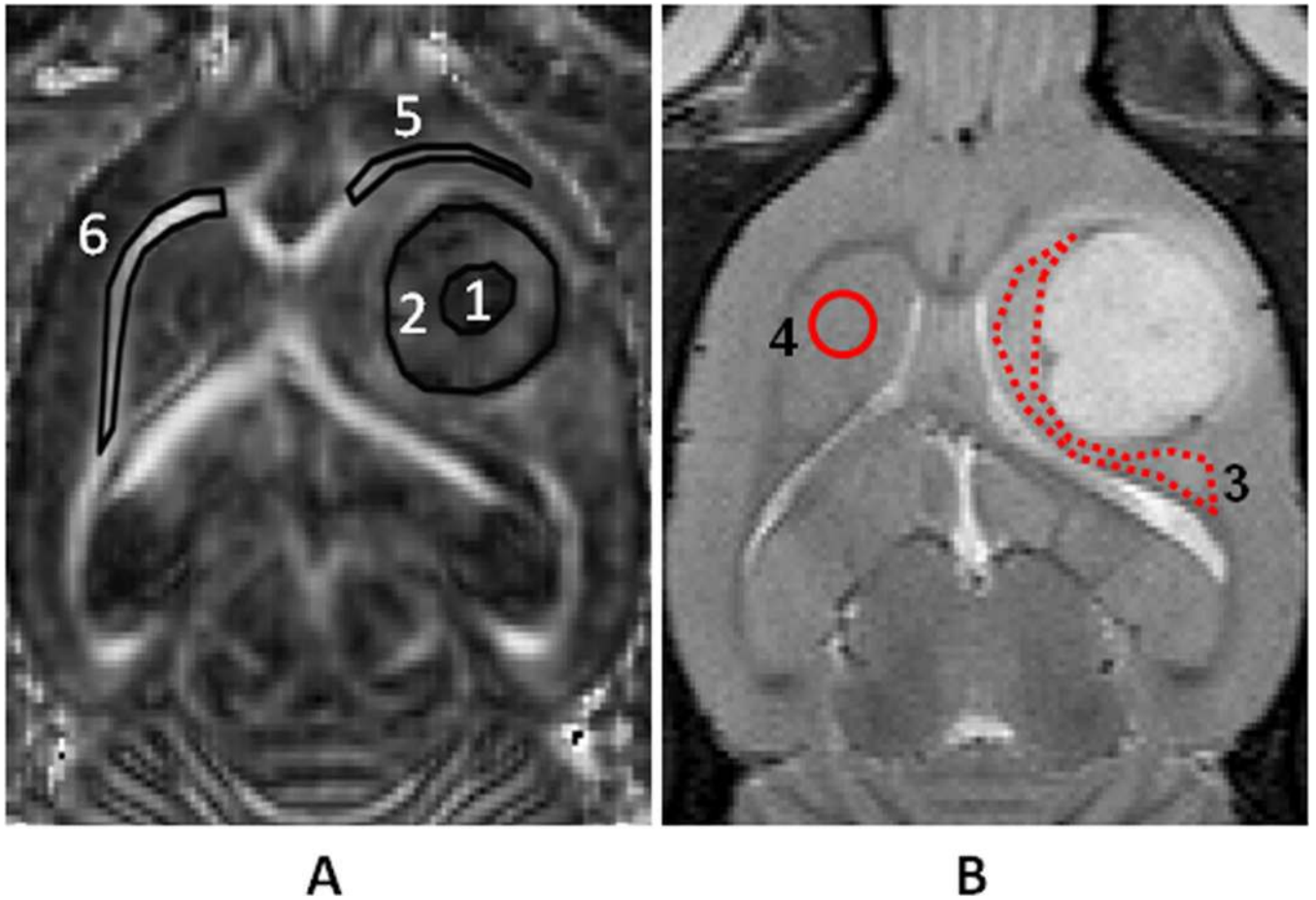
Fig 1.
Examples of ROIs in an FA map (A) and a T_2w image (B) from an F98 tumor. The ROIs over the FA map (A) include the tumor center (1), tumor rim (2), ipsilateral white matter (5), and contralateral white matter (6). Peritumoral edema (3) and contralateral grey matter (4) are defined on the T_2w image (B). These ROIs were transferred to identical sites on FA, ADC, $\lambda_{//}$, and $\lambda\perp$ maps.
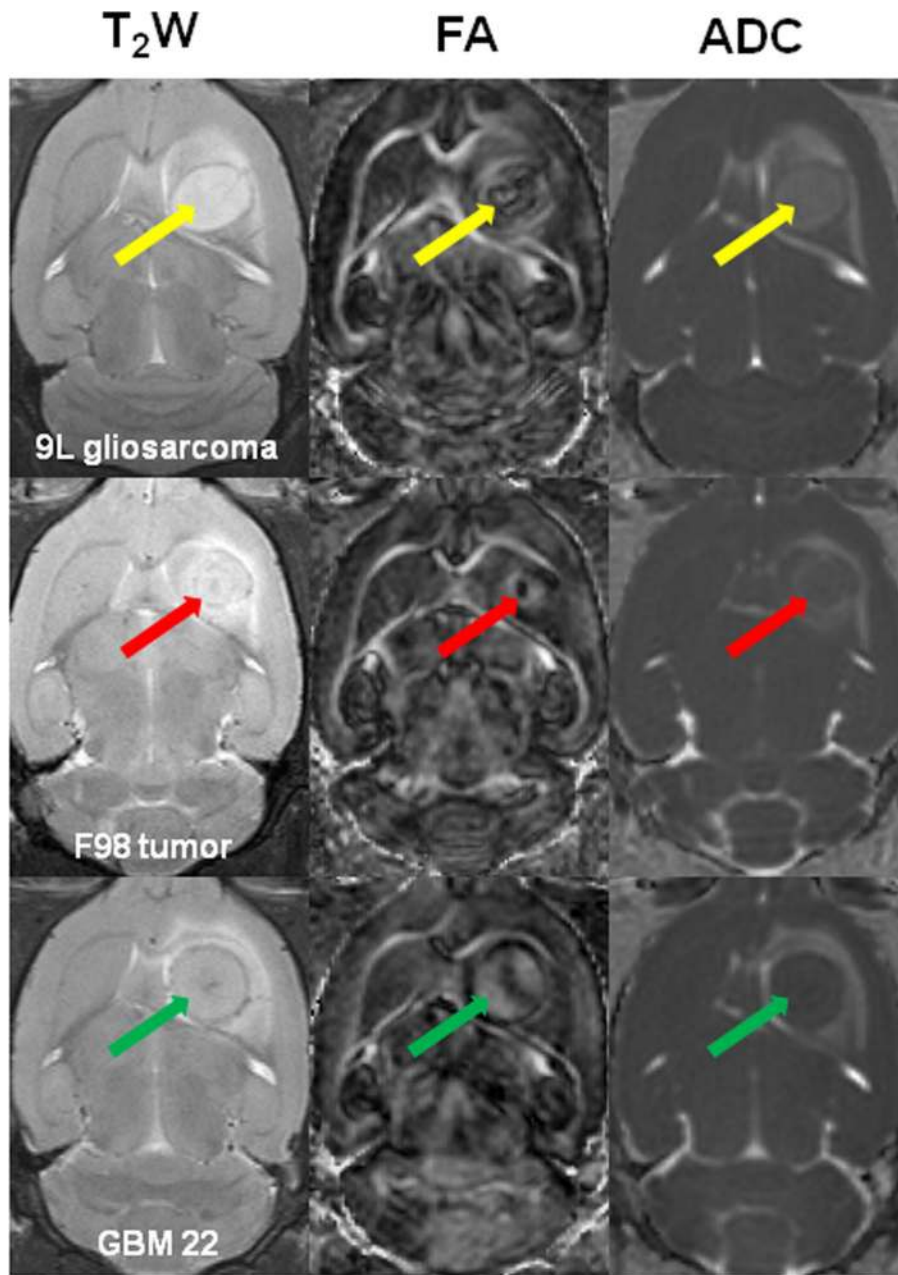
Fig 2.
T$_2$w and DTI imaging features of brain gliomas in animal models. On the conventional T$_2$w images, the tumors show hyperintensive regions with abnormally increased signals in the peritumoral edema. On the FA maps, there is a small dark central area with low diffusion anisotropy and a bright rim with a high degree of diffusion anisotropy for all tumors. On the ADC maps, the tumor regions show hyperintensity (9L gliosarcoma and F98 tumor) or iso-to hyperintensity (GBM22), compared to the contralateral grey matter. The peritumoral area has abnormally increased signals.
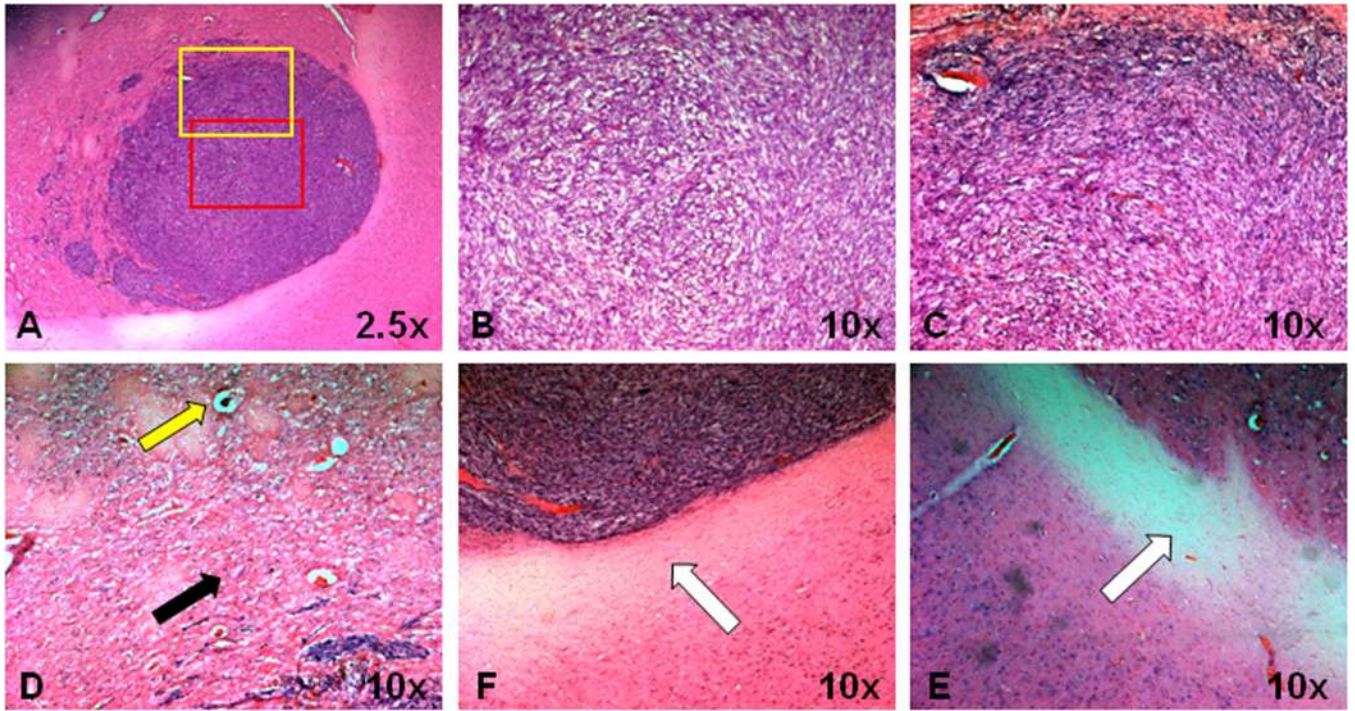
Fig 3.
Histological features of 9L tumor in a rat. A, Tumor mass is relatively homogeneous. B and C, Red and yellow rectangular tumor areas in (A) under 10× magnification. The orientation of tumor cells and the adjacent interstitial spaces form a circular pattern in the outer part of the tumor. D, Peritumoral edema shows compressed brain parenchyma (black arrow), dilated vessels (yellow arrow), as well as vacuolation changes. E and F, Ipsilateral adjacent white matter and contralateral white matter. Both white matter tracts appear normal and intact (white arrow).
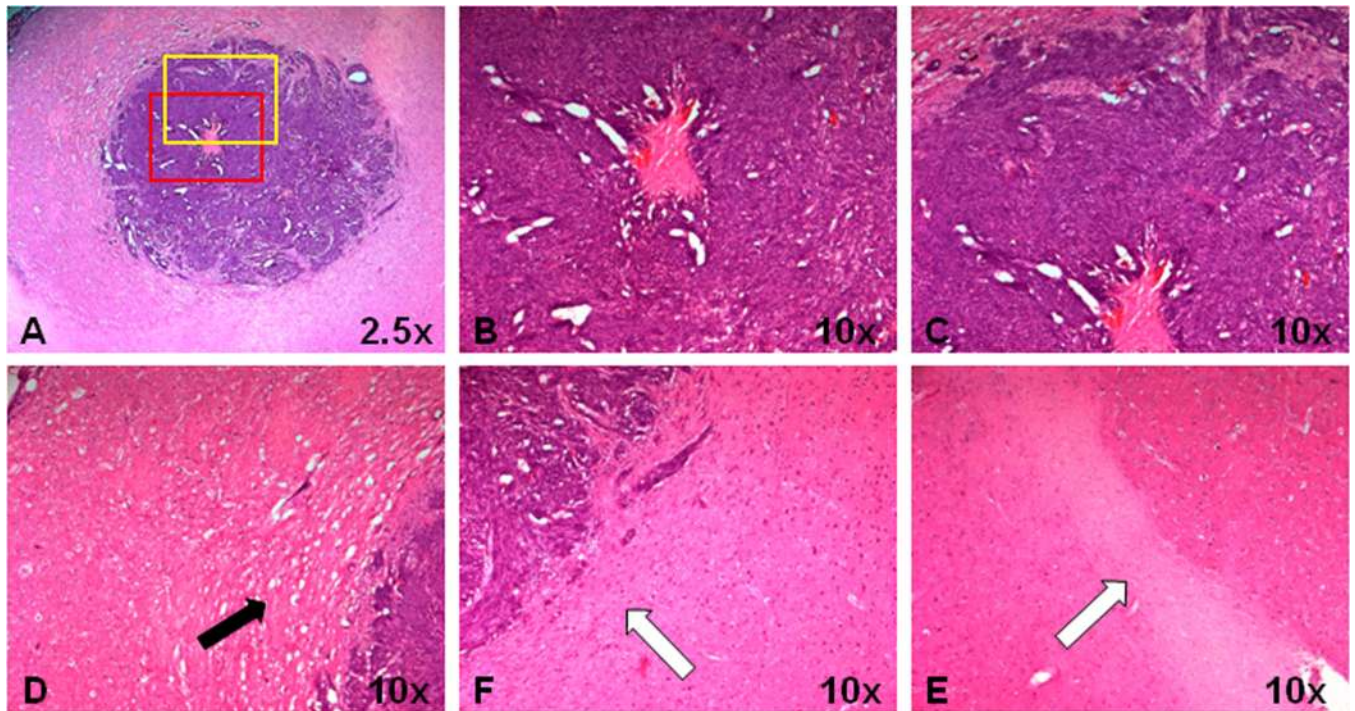
Fig 4.
Histological features of an F98 tumor in a rat. A, F98 tumor shows heterogeneous tumor mass with central necrosis. B and C, Red and yellow rectangular tumor areas in (A) under 10× magnification. The orientation of tumor cells and the adjacent interstitial spaces form a circular pattern in the outer part of the tumor. D, Peritumoral edema shows compressed brain tissue (black arrow) without obvious tumor invasion. E and F, Ipsilateral adjacent white matter and contralateral white matter. Both sides of the white matter tracts seem normal and intact (white arrow).
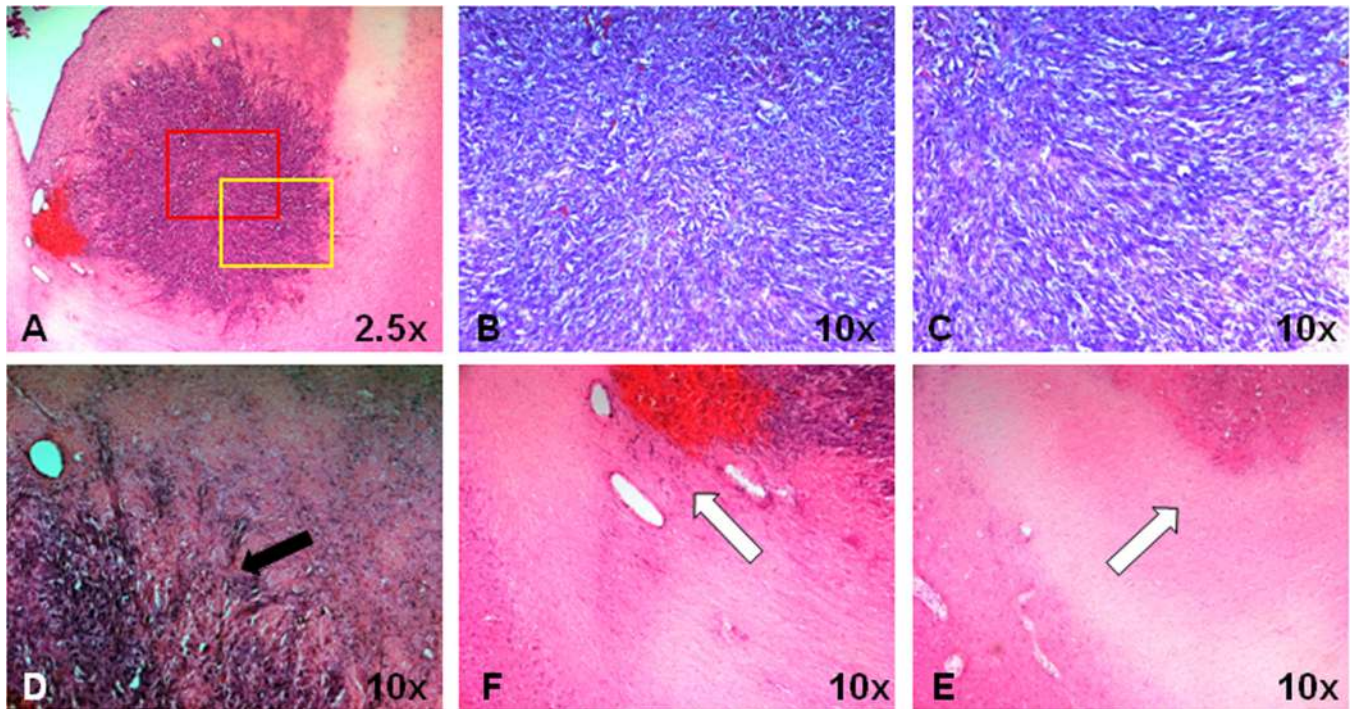
Fig 5.
Histological features of a GBM22 tumor xenograft in a rat. A, GBM22 tumor shows a heterogeneous tumor mass with central necrosis. B and C, Red and yellow rectangular tumor areas in (A) under 10× magnification. There are highly coherent, radially organized tumor cells and adjacent interstitial spaces in the outer part of the tumor. D, Tumor cells infiltrate the adjacent brain parenchyma (black arrow). E and F, Ipsilateral adjacent white matter and contralateral white matter. Tumor cells infiltrate the adjacent ipsilateral white matter.

Table 1

Quantitative analysis of DTI indices in 9L, F98, and GBM22 glioma animal models

	9L (n=8)		F98 (n=5)		GBM22 (n=8)	
	Tumor center	**Tumor rim**	**Tumor center**	**Tumor rim**	**Tumor center**	**Tumor rim**
FA	0.32 ± 0.06	0.39 ± 0.08	**0.22 ± 0.11**	**0.33 ± 0.10**[**]	**0.22 ± 0.06**	**0.37 ± 0.07**[**]
ADC (10^{-3}mm^2/s)	1.06 ± 0.13	1.00 ± 0.13	0.87 ± 0.04	0.87 ± 0.05	0.96 ± 0.21	0.98 ± 0.20
$\lambda_{//}$ (10^{-3}mm^2/s)	1.39 ± 0.13	1.43 ± 0.25	1.06 ± 0.05	1.10 ± 0.09	**1.03 ± 0.15**	**1.27 ± 0.27**[**]
$\lambda\perp$ (10^{-3}mm^2/s)	**0.90 ± 0.13**	**0.79 ± 0.10**[*]	**0.78 ± 0.07**	**0.71 ± 0.06**[*]	0.84 ± 0.21	0.79 ± 0.19

	Peritumoral Gray matter	**Contralateral Grey matter**	**Peritumoral Gray matter**	**Contralateral Grey matter**	**Peritumoral Gray matter**	**Contralateral Grey matter**
FA	0.34±0.02	0.30±0.04	0.27±0.09	0.28±0.07	0.33±0.04	0.27±0.05
ADC (10^{-3}mm^2/s)	**1.02±0.08**	**0.78±0.16**[*]	**0.90±0.08**	**0.71±0.06**[**]	**1.01±0.08**	**0.77±0.03**[**]
$\lambda_{//}$ (10^{-3}mm^2/s)	**1.40±0.17**	**1.16±0.20**[*]	**1.15±0.11**	**0.93±0.05**[*]	**1.37±0.12**	**0.82±0.08**[**]
$\lambda\perp$ (10^{-3}mm^2/s)	**0.84±0.08**	**0.64±0.07**[**]	**0.77±0.09**	**0.60±0.08**[**]	**0.89±0.13**	**0.73±0.16**[**]

	Peritumoral white matter	**Contralateral white matter**	**Peritumoral white matter**	**Contralateral white matter**	**Peritumoral white matter**	**Contralateral white matter**
FA	0.44±0.06	0.49±0.06	0.51±0.07	0.47±0.04	**0.39±0.07**	**0.54±0.06**[**]
ADC (10^{-3}mm^2/s)	0.79±0.01	0.74±0.03	0.78±0.11	0.70±0.02	**1.09±0.27**	**0.86±0.15**[*]
$\lambda_{//}$ (10^{-3}mm^2/s)	1.27±0.10	1.29±0.08	1.21±0.09	1.19±0.07	1.45±0.31	1.28±0.23
$\lambda\perp$ (10^{-3}mm^2/s)	0.55±0.05	0.57±0.03	0.54±0.04	0.53±0.06	**0.81±0.23**	**0.55±0.07**[*]

Paired sample t-test was used to compare the significance of the differences. Significant statistical differences are labeled in bold.

[*]
p < 0.05,

[**]
p < 0.01.